Engineering Geology 201 (2016) 57–66

Contents lists available at ScienceDirect

Engineering Geology

journal homepage: www.elsevier.com/locate/enggeo

Deep characterization of the Santiago Basin using HVSR and cross-correlation of ambient seismic noise

C. Pastén *, M. Sáez, S. Ruiz, F. Leyton, J. Salomón, P. Poli

ARTICLE INFO

Article history:
Received 30 August 2015
Received in revised form 14 December 2015
Accepted 19 December 2015
Available online 23 December 2015

Keywords:
Cross-correlation
Noise correlation function
Shear wave velocity
Seismic characterization
Dispersion curve
Broadband station
HVSR

ABSTRACT

Continuously recorded seismic ambient noise is used to investigate the intermediate and deep structure of the Santiago Basin for seismic site-response evaluation. Single-station H/V spectral ratios (HVSR) were used as a proxy to identify zones with high stiffness soils and low impedance contrast with the underlying bedrock, as a complement of available surface geology information. Frequency-domain cross-correlation of the vertical components of ambient noise were calculated and used to estimate phase velocity dispersion curves associated to station pairs over different soil deposits. In addition, noise correlation functions (NCFs) calculated from time-domain cross-correlation of the vertical seismic noise records were used to estimate group velocity dispersion curves and to verify results from the spectral method. Data processing from both methods resolves a frequency band between 0.1 and 8.0 Hz, a critical band for civil infrastructure that is difficult to determine with traditional local-scale passive surface wave methods. Station pairs with high signal correlation over stiff soils in the center, south, and east part of the basin, mainly associated to flat HVSR response, yielded robust phase velocity dispersion curves that vary approximately from 3.5 km/s at 0.1 Hz to 1 km/s at 4 Hz. Shear wave velocity profiles inverted from the dispersion curves show high average shear wave velocities that also have a pronounced increase rate with depth and a lack of clear soil-bedrock interface at depths predicted by available gravimetric data.
© 2015 Elsevier B.V. All rights reserved.

1. Introduction

The Santiago Basin (Fig. 1) concentrates more than 40% of the Chile's population, along with most of the critical infrastructure of the country. This area is located in a subduction zone where large earthquakes frequently occur (Leyton et al., 2010; Udias et al., 2014). Two large earthquakes affected the urban structure of the Santiago city during the last thirty years, the 1985 Mw 8.0 Valparaiso and the 2010 Mw 8.8 Maule earthquakes. The earthquakes' Medvedev–Sponheuer–Karnik (MSK) scale intensities in the Santiago metropolitan area ranged between VI and VIII and were mainly associated to the surface geology characteristics (Leyton et al., 2011; Astroza et al., 2012).

The seismic response of a soil deposit depends on its shear wave velocity profile, which can be directly measured from invasive in-situ tests or estimated from the dispersive characteristics of surface waves propagating through it. The stiff and strong soils deposited in the metropolitan Santiago area complicate the use of traditional invasive in-situ tests, such as down-hole and cross-hole tests, that could measure properties of the deepest soil layers. In fact, no single borehole has been drilled to reach the contact with the underlying bedrock. On the other hand, the use of noninvasive geophysical methods based on active sources, such as multichannel analysis of surface waves (MASW) and spectral analysis of surface waves (SASW), and passive sources, such as spatial autocorrelation (SPAC) and refraction microtremor (Remi), are limited by the source energy required to reach the deeper soil layers and by restrictions on the maximum distance between receivers, respectively.

Another method used to study the elastic structure of a soil deposit is the cross-correlation of ambient seismic noise recorded at two receivers. A phase velocity dispersion curve can be calculated from the spectral method based on Aki's formulation (Aki, 1957; Ekström et al., 2009; Tsai and Moschetti, 2010; Boschi et al., 2013). The ensemble averaged real part of the two-station coherence function, or cross-correlation spectrum, approximates a zero-order Bessel function of the first kind (J_0) (Aki, 1957; Sánchez-Sesma and Campillo, 2006). In the time domain, the zero-order Bessel function is the medium's Green Function and can be estimated from the ensemble average cross correlation of ambient noise. An approximation of the surface wave part of the Green's function, or empirical Green's function (EGF), can be estimated from the time-derivative of the time-averaged ambient noise correlation function (NCF) between long continuous time records at two stations (Shapiro and Campillo, 2004; Poli et al., 2012; Boschi et al., 2013). EGFs and NCFs have been used to study features of the Earth structure (Shapiro and Campillo, 2004; Poli et al., 2012), as well as to determine wave velocity distribution at continental (Shapiro et al., 2005; Bensen et al., 2007; Yang et al., 2007; Ward et al., 2013) and basin scales (Nunziata et al., 2009; Picozzi et al., 2009; Boaga et al., 2010; Hannemann et al., 2014; Mordret et al., 2014).

Dispersion curves can be estimated from spectral and time-domain methods and shear wave velocity profiles can be calculated by

* Corresponding author.

http://dx.doi.org/10.1016/j.enggeo.2015.12.021
0013-7952/© 2015 Elsevier B.V. All rights reserved.

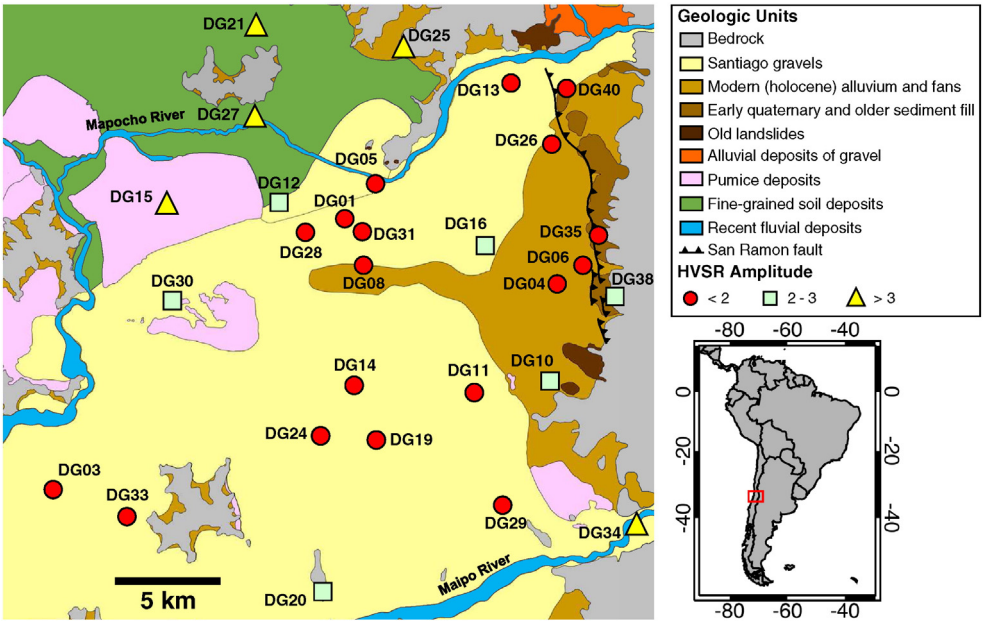

Fig. 1. Broadband stations in the Santiago basin. Colors correspond to surface geology (Leyton et al., 2011) and symbols indicate the location of the broadband stations as well as results from HVSR.

traditional inversion methods (Sabra et al., 2005; Yao et al., 2006; Ekström et al., 2009). While the frequency-domain method resolves wavelengths in the order of the interstation distance, the time-domain method can be used to calculate group velocities at higher frequencies (Boschi et al., 2013).

In the present study, we deployed a temporal network of broadband seismological stations throughout the Santiago Basin to perform intermediate to deep soil structure characterization. First, we describe the seismic network and explain how we used the HVSR method to classify the sites. Then, we show the processing method of the vertical components of ambient seismic noise to estimate cross-correlation in the time- and frequency-domains. Later, we present phase and group velocity dispersion curves and the most representative shear wave velocity profiles of three city districts. Finally, we discuss our results in view of available data and about the implications on the seismic site response of the basin.

2. Geological setting

The Santiago Basin is located in the intermediate depression of central Chile surrounded by the Coastal Cordillera in the west and the Andean Cordillera in the east. While the Coastal Cordillera is composed of Jurassic to upper Cretaceous volcanic and sedimentary sequences and Jurassic to cretaceous intrusive rocks, the Andean Cordillera is mainly composed of volcanic and sedimentary sequences deposited during Cenozoic in Abanico intra-arc basin (Charrier et al., 2002). The sedimentary cover of the basin is relatively shallow and flat with 250 m of average depth and three depocenters that reach approximately 600 m, one of which is in the north-eastern side and the other two in the south-west side of the basin (Yañez et al., 2015).

The coalescence of the Mapocho and Maipo rivers filled the Basin with alluvial sediments, known as the Santiago gravels (Fig. 1), composed primarily of gravel and pebbles of high strength and stiffness (Bonnefoy-Claudet et al., 2009; Pilz et al., 2010). No single borehole in the gravelly deposit has reached the contact with the underlying bedrock and only one study attempted to estimate deep shear wave velocity profiles inverting HVSR in the center of the basin (Pilz et al., 2010). These stiff soil deposits complicate the use of invasive in-situ tests to measure properties of the deepest soil layers, and the limited source energy associated to active geophysical methods hampers the proper characterization of the sediments/bedrock contact.

The north of the basin consists of softer fine-grained-soils (Fig. 1) that create a large impedance contrast with the basement rock, and that can easily be investigated with traditional exploration methods, such as MASW, SASW, and SPAC. Towards the west of the basin, there are pyroclastic deposits, known as Pudahuel Ignimbrite, composed of rhyolitic tuffs that merge with northern fine-grained soils and the Santiago gravels towards the basin central part (Stern et al., 1984). These deposits have variable thickness and stiffness (Rebolledo et al., 2006). On the other hand, the east part of the basin is filled with alluvial deposits that are composed of boulders, gravels, and fine-grained soils in intricate structures and dominated by mudflows and fans (Armijo et al., 2010).

3. Database

The seismic network deployed in the Santiago basin consists of 29 stations, each one equipped with a broadband Trillium compact 120 s-period sensor, a 24-bit Quanterra Q330 digitizer, a Marmot data logger system (Kinemetrics), and a GPS antenna. The stations recorded in continuous time in the north–south (NS), the east–west (EW), and the vertical (Z) directions at a rate of 100 samples per second. The network installation started in July 2013 and operated until May 2014. Fig. 1 shows the location of the broadband stations in the basin along with the surface geology.

4. Site characterization with HVSR

Site characterization obtained from surface geology is complemented with H/V spectral ratios (HVSR), which were calculated using the software Geopsy® (available at www.geopsy.org) using 60 s temporal windows of the recorded stationary noise, free from transient. The criterion to detect transients is based on the comparison between the average signal amplitude over a short time period $t_{STA} = 1$ s, STA, and the average signal amplitude over a longer time period $t_{LTA} = 60$ s, LTA. Windows with STA/LTA ratio between 0.5 and 2 are considered as stationary noise and used for HVSR computation. For every selected time window, the Fourier amplitude spectra of the two horizontal and the vertical components are smoothed with a Konno and Ohmachi (1998)

filter using a bandwidth coefficient b = 40 before dividing the quadratic mean of the horizontal amplitude spectra by the vertical one. The final HVSR is obtained by averaging the H/V amplitudes from all selected windows, and the standard deviations values for every frequency are estimated from the H/V amplitude logarithm. The selected calculation parameters follow the recommendations of the SESAME consortium (Bard and SESAME-Team, 2004).

Fig. 2 shows examples of HVSRs from five days of stationary noise recorded at the broadband stations. The solid black line in the figures is the result of averaging all available HVSR windows at each site and the shaded area represents the associated standard deviation. The one-minute selected windows used to calculate HVSR in the 29 stations ranged between 97 and 4860 (details in Table S1, Supplementary Material) and resulted in very stable average HVSR curves. For simplicity, we classified HVSRs in flat (H/V amplitudes smaller than 2.0 – Fig. 2a), subtle peak (H/V amplitudes between 2.0 and 3.0 – Fig. 2b), and clear peak (H/V amplitudes larger than 3.0 – Fig. 2c). The distribution of the HVSR types in the basin is shown in Fig. 1. The HVSRs over the Santiago gravel and the eastbound alluvium are mainly dominated by flat responses (Fig. 2a), whereas the north fine-grained deposits are characterized by spectral ratios with larger peak amplitudes (Fig. 2b and c). HVSR in all stations are shown in Fig. S1, and the HVSR peak amplitudes and their corresponding frequencies are reported in Table S1.

Previous studies have shown that a large-amplitude HVSR peak can be associated to a high impedance contrast between the sedimentary cover and the basement, while a low amplitude peak relates to a lower contrast, indicating the presence of a stiff soils (Bonnefoy-Claudet et al., 2006, 2009; Leyton et al., 2013).

A few sites exhibited subtle peaks at frequencies that do not agree with the fundamental frequency predicted by the one-dimensional vertical shear wave propagation theory, f = Vs/(4 H) (where Vs is the soil deposit shear wave velocity and H is its thickness). Meanwhile, other sites in the center of the basin show HVSR with two peaks probably attributed to the predominant frequency of the entire soil deposit at the lowest frequency and the shallower soil layers, such as pumice and fine grained-soils, at higher frequencies. This information is only used as a proxy to identify sites with more complex stratigraphy.

5. Data processing

The data processing technique adopted in this study attempts to improve resolution at frequencies lower than the frequencies solved by traditional surface wave methods and to capture wavelengths in the order of the sedimentary cover thickness (from 100 to 1000 m). We explore frequency- and time-domain cross-correlations to obtain the dispersive properties of fundamental-mode Rayleigh waves that travel between pair of stations.

5.1. Frequency-domain method: determination of phase velocity

The data processing of the frequency-domain method follows the next steps (Ekström et al., 2009; Ekström, 2014):

(i) The continuous daily vertical records are visually inspected, high-pass filtered with a fourth-order Butterworth filter of cutoff frequency at 0.01 Hz to remove the trend and the mean, and divided in ten-minutes windows.
(ii) The Fourier spectra of the records at two stations and the cross-correlation spectrum between them are calculated in each window.

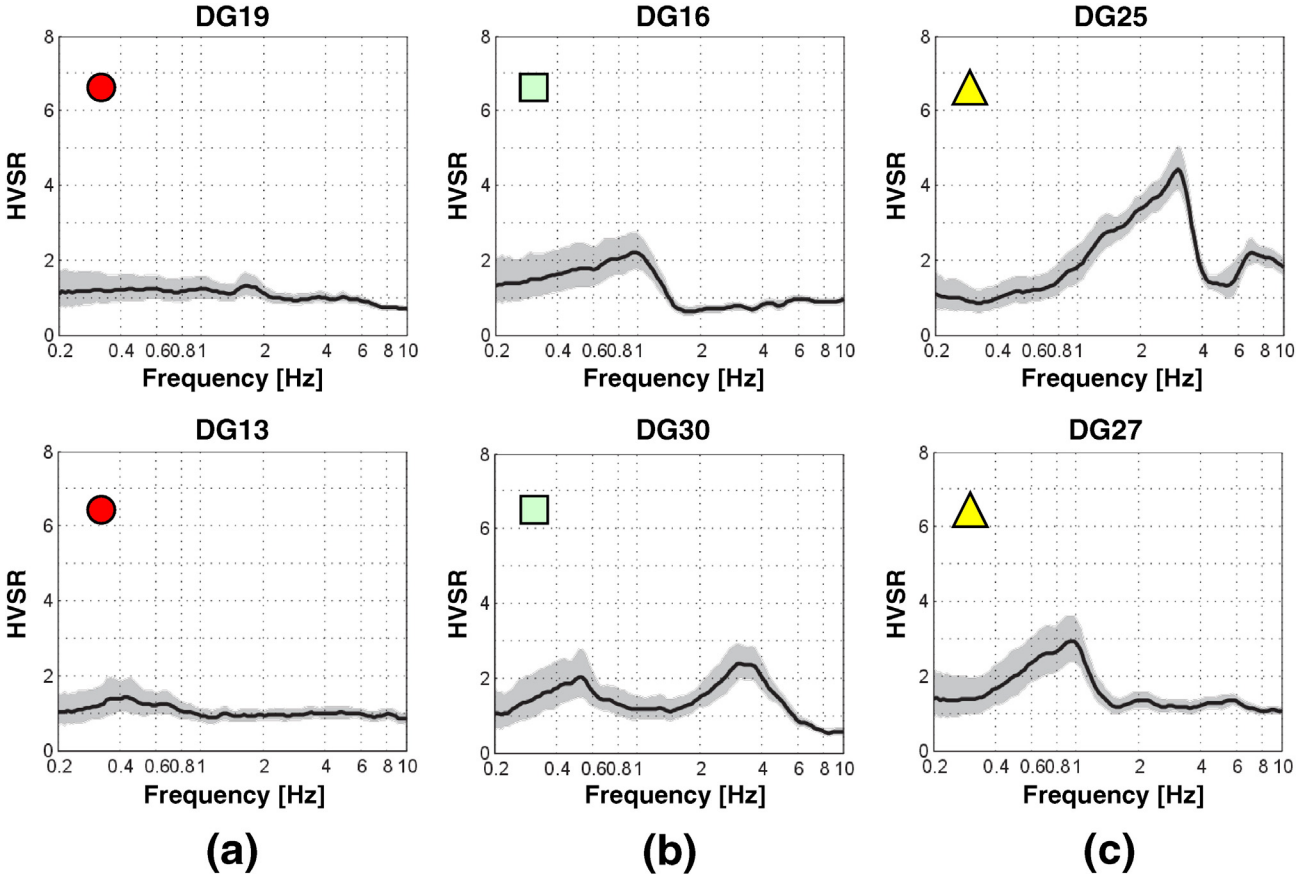

Fig. 2. Single-station H/V spectral ratios of the broadband seismic network. Examples of (a) flat spectral ratios (H/V amplitude <2), (b) spectral ratios with subtle peak (2 ≤ H/V amplitude <3), and (c) spectral ratios with clear peak (H/V amplitude ≥3). The solid black line is the result of averaging all HVSR windows with stationary noise at each site and the shaded area represents the associated standard deviation.

(iii) The real component of the cross-correlation spectrum is stacked after normalizing by the maximum absolute value.
(iv) The ensemble average cross-correlation spectrum is plotted as a function of frequency, and the zero-crossing frequencies are identified to later associate them to the zero crossings of the zero-order Bessel function of the first kind (J_0). Fig. 3a shows the real part of the cross-correlation spectra in 44 days-span and the final spectrum obtained after stacking (Fig. 3b). The spectral shape is rather stable, which suggests that fewer days of records could have similar results.
(v) The phase velocity $c(\omega_n)$ [m/s] is calculated from the interstation distance Δ [m], the frequencies of the function zero crossings ω_n [rad/s], and the value of the zero crossing of the J_0 function z_{n+m} as

$$c(\omega_n) = \frac{\omega_n \cdot \Delta}{z_{n+m}} \quad (1)$$

where m is the number of missed or extra zero crossings. This equation yields a family of curves depending on the m-value adopted and from which the most physically-meaningful must be chosen as the dispersion curve. In most cases, the m-value that results in a curve that plateaus near 3.5 km/s at 0.1 Hz is considered (Fig. 3c). Fig. 4 shows a flowchart that summarizes the frequency-domain method.

5.2. Time-domain method: determination of group velocity

The time-domain analysis aims to find noise correlation functions (NCFs) between two stations. The methodology can be summarized as follows:

(i) The continuous daily vertical records are visually inspected, high-pass filtered with a cutoff frequency of 0.01 Hz to remove the trend and the mean, and divided in ten-minutes windows.
(ii) Time-domain noise correlation functions (NCF) are calculated in every time window.
(iii) The resulting NCFs are band-pass filtered using fourth-order Butterworth filters with three center frequencies per octave

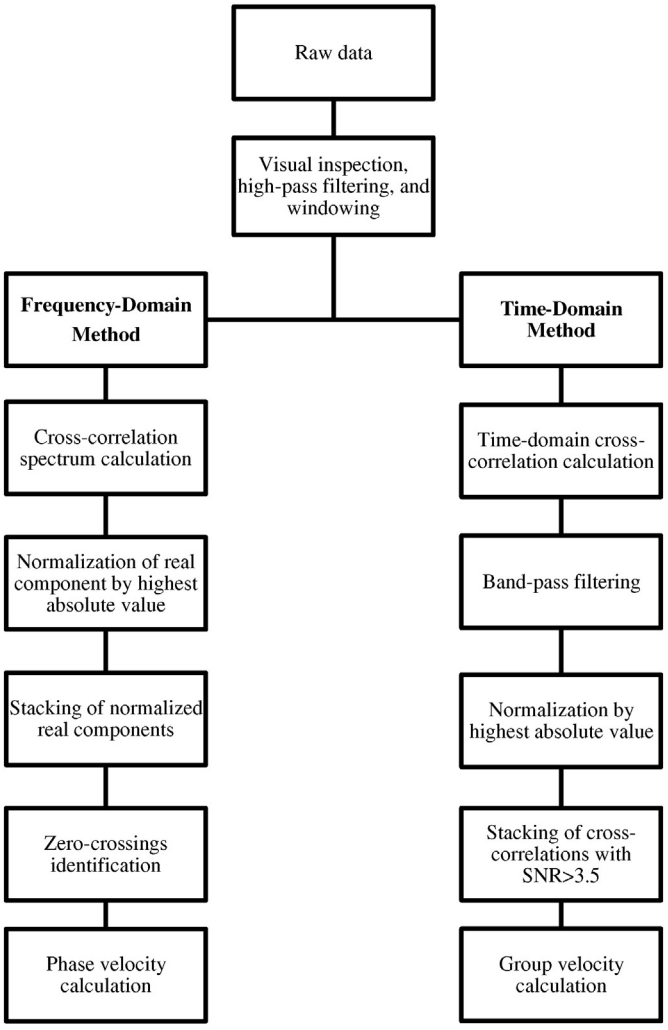

Fig. 4. Flowchart of the frequency- and time-domain methods to determine ambient noise cross-correlations.

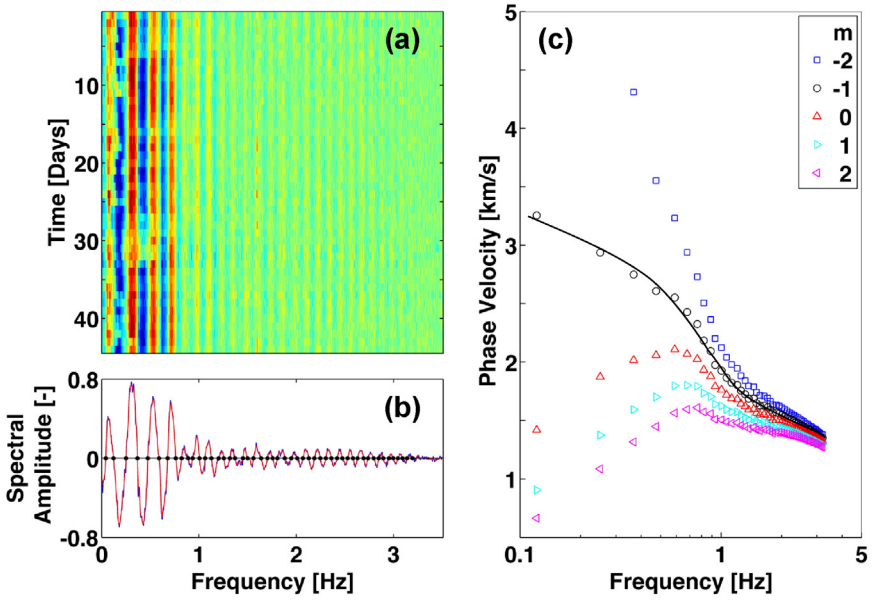

Fig. 3. Phase velocity from spectral-method. (a) Color map of the real component of the cross-power spectrum after daily stacking of 10 min windows for 44 days, (b) stacked real component of the cross-power spectrum, and (c) dispersion curves calculated with Eq. (1) for different m-values. The continuous line indicates the dispersion curve chosen in this example.

(fc = 0.18, 0.25, 0.35, 0.5, 0.71, 1.0 Hz) and a half bandwidth of 15% of the center filter frequency for frequencies lower than 1 Hz, and four center frequencies per octave (fc = 1.26, 1.59, 2.0, 2.52, 3.17, 4.0, 5.04, 6.35, 8.0 Hz) and a half bandwidth of 12% of the center filter frequency for frequencies larger than 1 Hz. The chosen center filter frequencies and bandwidths ensure adequate discretization in the frequency domain and reduce the influence of highly energetic low-frequency waves at frequencies larger than 1 Hz.

(iv) The filtered traces at different center frequencies in every window are normalized by their respective highest absolute values.

(v) The normalized traces at a given center frequency with high signal-to-noise ratios SNR are stacked. The SNR is calculated as the ratio of the trace peak value to the root mean square of the trace elsewhere. A minimum SNR = 3.5 ensures that enough windows are selected for stacking and clearly improves SNR of high center frequencies NCF. A similar stacking approach is implemented in Picozzi et al. (2009) and Shirzad and Shomali (2014) in terms of the traces' root mean square.

Group velocity for a given center frequency $V_g(f_c)$ is directly calculated from the interstation distance Δ [m] and the time t_p [s] at which the NCF peaks as

$$V_g(f_c) = \frac{\Delta}{t_p} \tag{2}$$

Fig. 4 shows a flowchart that summarizes the time-domain method.

5.2.1. Comments on the time-domain method

A ten-minute window is adequate to capture the frequency range of interest in this study (see an example in Shirzad and Shomali, 2014), and it increases the number of segments considered for stacking, which improves the SNR of the resultant NCFs. The use of a SNR criterion and selection of multiple windows reduce the influence of earthquakes that may affect the final NCFs, avoiding the use of spectral whitening and time normalization (Ekström, 2014). Due to anthropic activity, such as traffic, fewer windows satisfied the adopted SNR criterion at center filter frequencies larger than 2 Hz; and consequently, fewer windows were considered in the resulting NCF at high frequencies.

The minimum analyzed frequency f_{min} with this method is such that the maximum wavelength $\lambda_{max} = V_{av}/f_{min}$ is smaller than a third of the interstation distance Δ:

$$f_{\min} = 3\left(\frac{V_{av}}{\Delta}\right) \tag{3}$$

where V_{av} [m/s] is the average group velocity for the center filter frequency f_{min} [Hz]. Since V_{av} is not known beforehand, f_{min} is computed after the calculation of the entire soil profile.

We compared group velocity dispersion curves calculated following the described time-domain method and the velocities obtained by applying the S-Transform (Stockwell et al., 1996) to the raw time-domain cross-correlation function. The latter method calculates the group velocity from the time associated to the peak of the normalized time-frequency representation of the cross-correlation (i.e., the normalized S-Transform) and the interstation distance. Both methods yield similar group velocities in the frequency range of interest, which validates our approach (see an example in Fig. S2).

6. Results

The deep structure of the Santiago basin between pairs of stations was investigated by calculating the cross-correlation of the vertical continuous records using the frequency- and time-domain methods. The records at some stations show strong correlation, which results in cross-correlation spectra with clear and regular zero-crossing frequencies (Fig. 5a) and high signal-to-noise ratio (SNR) NCFs in the time domain (Fig. 5b). In contrast, station records that poorly correlate have spectra with zero-crossings difficult to identify (Fig. 5c) and low SNR NCFs (Fig. 5d). Fig. 6 shows the distribution of station pairs with strong and poor correlation. Strong noise correlation was found between pairs of stations over the Santiago gravel and stiff soils with flat HVSR whereas poor correlation is associated to stations over fine-grained soils and ignimbrite deposits that have larger HVSR amplitudes. We hypothesize that strong local vibration characteristics hinder the effect of coherent surface wave fronts travelling through stations with high amplitude HVSR.

Directivity is easily captured in the time-domain cross-correlations. Fig. 6 also shows station pairs with prevalent directionality based on time-domain analysis. Anti-symmetric NCFs with higher SNR in the anti-causal part (negative time-lags) are found in stations over stiff soils near the east boundary of the basin. We believe the symmetry is altered by noise sources generated preferably within the basin rather than outside and enhanced by the presence of the San Ramon thrust fault in this zone (Armijo et al., 2010) that may cause discontinuous wave velocity profiles (Díaz et al., 2014). Since seismic amplification can be controlled in different directions by the presence of shallow faults (Panzera et al., 2014), more research is required to properly interpret our observations.

Based on these results, we analyzed three zones where we had the densest station coverage and distinctive surface geology: central, east, and south districts (boxes in Fig. 6). In every district, we calculated phase- and group-velocities with the frequency- and the time-domain methods and found the most representative shear wave velocity profiles.

6.1. Central district

The Central district is over the Santiago gravel, and it concentrates most of the government buildings, commerce, and population density of the city (see black box in Fig. 6). Fig. 7a shows phase velocities calculated with the frequency-domain method as a function of frequency. Pairs of stations with high noise correlation and interstation distances shorter than 5 km allowed solving phase velocities up to 5 Hz. The figure shows phase velocities decreasing from 2.8 km/s at 0.3 Hz to 1 km/s at 5 Hz. Additional station pairs using stations DG30 and DG15 were used to find that the phase velocity increases asymptotically to 3.4 km/s at frequencies near 0.1 Hz.

6.2. East district

The East district is over Santiago gravel and modern alluvium (see black box in Fig. 6). Fig. 7b shows phase velocities calculated with the frequency-domain method as a function of frequency. The interstation distances allowed solving velocities up to 3.5 Hz. The figure shows phase velocities lying in a narrow band, decreasing to 1 km/s, approximately. Additional pairs with stations DG05, DG08, DG28, and DG31 were explored to resolve lower frequencies in the zone.

6.3. South district

The South district is located over the Santiago gravel in the south of the basin (see black box in Fig. 6). Fig. 7c shows phase velocities calculated with the frequency-domain method as a function of frequency. Pairs of stations with interstation distances smaller than 12 km allowed solving phase velocities up to 4 Hz. The pairs displayed in the figure have dispersion curves that fall in a narrow band above the central- and east-district trends. The figure shows phase velocities decreasing to an average phase velocity of 1.3 km/s at 4 Hz. Additional station

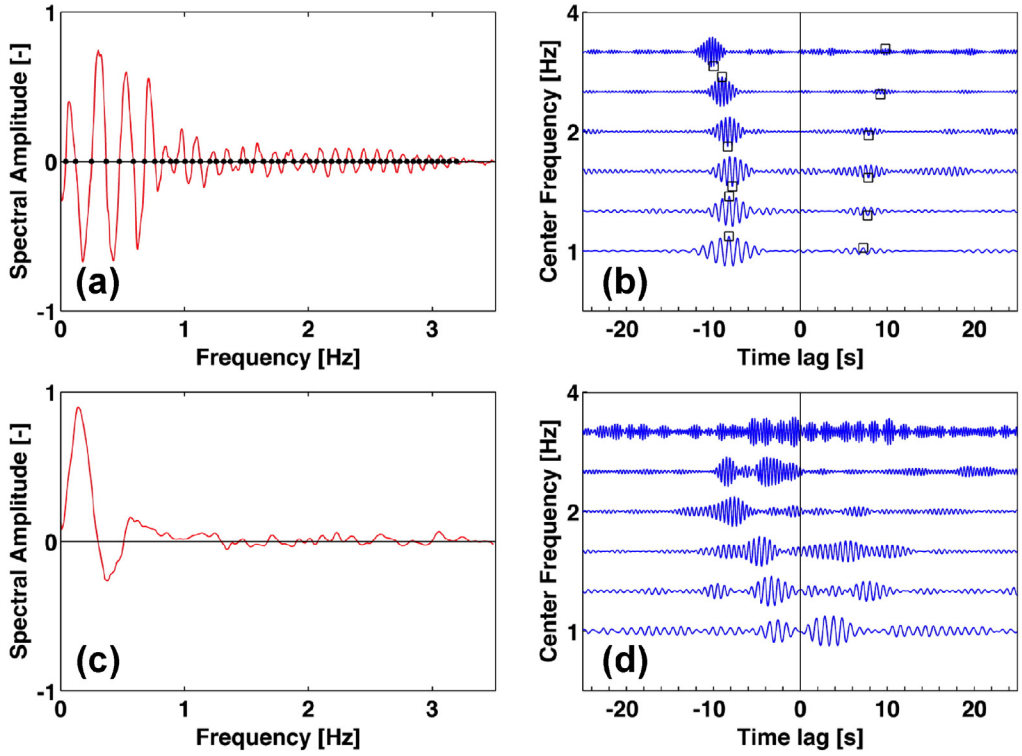

Fig. 5. Examples of cross-correlation in time- and frequency-domains. Station pair with high noise correlation (DG24-DG29, inter-station distance = 10.3 km): (a) Real part of the cross-correlation spectrum and (b) noise correlation functions at various center frequencies. Open squares show the functions peak amplitudes. Station pair with low noise correlation (DG21-DG25, inter-station distance = 7.8 km): (c). Real part of the cross-correlation spectrum and (d) noise correlation functions.

pairs using stations DG03, DG33, DG20, and DG34 were used to solve lower frequencies.

Average phase velocity dispersion curves are drawn in Fig. 7 to capture the trend in all the districts. The curves were calculated from individual station-pairs adjusted curves, resampled at even frequencies.

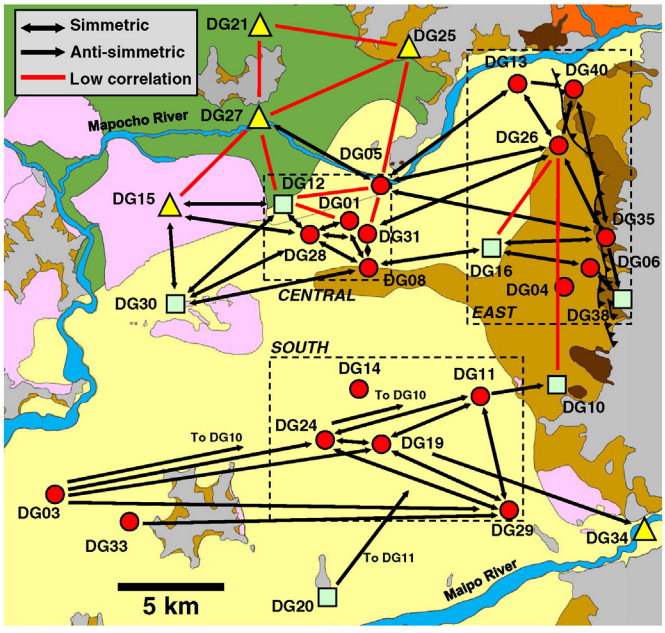

Fig. 6. Correlation between station pairs in the Santiago Basin. Not all the analyzed pairs are displayed for clarity. Symmetric and anti-symmetric refer to differences in SNR of causal and anticausal parts of NCFs in the time domain. The arrows point in the direction of larger SNR. Boxes drawn with dotted lines represent the districts where the dispersion curves and shear wave velocity profiles are determined.

These curves are inverted in the following section to find characteristic shear wave velocity profiles for each district.

6.4. Comparison of frequency- and time-domain methods

Phase velocities calculated using the frequency-domain method can be converted to group velocity using

$$V_g(\omega_n) = \left[\omega \frac{\partial}{\partial \omega}\left(\frac{1}{c(\omega)}\right) + \frac{1}{c(\omega)}\right]^{-1} \quad (4)$$

which can be compared to the group velocities obtained from the time-domain analysis. Since calculation of group velocity is very sensitive to the slope of the phase velocity dispersion curve, we used smoothed curves to evaluate the Eq. (4).

Fig. 8 shows group velocities calculated using the time-domain method and group velocities computed with the Eq. (4) and the smooth trend of the phase velocity dispersion curve calculated with the frequency-domain method (Note: the NCFs of the station pair in this example are shown in Fig. 5b and the group velocity is calculated as the average between the causal and anti-causal parts of the NCF). The frequency-domain method resolves better lower frequencies, but both methods result in similar group velocities between 1 and 3.2 Hz. Based on this result, whenever the time-domain method is able to solve higher frequencies (Tsai and Moschetti, 2010), the phase velocity dispersion curve can be completed using the integral form of the Eq. (4) at higher frequencies. Similar results between phase and group velocities have been reported in Luo et al. (2015).

Fig. 9 compares group velocities of selected station pairs calculated using the time-domain method and the group velocity obtained applying Eq. (4) to the smooth trend phase velocity dispersion curves in Fig. 7. The analytical group velocity curve can be considered as an average of the data.

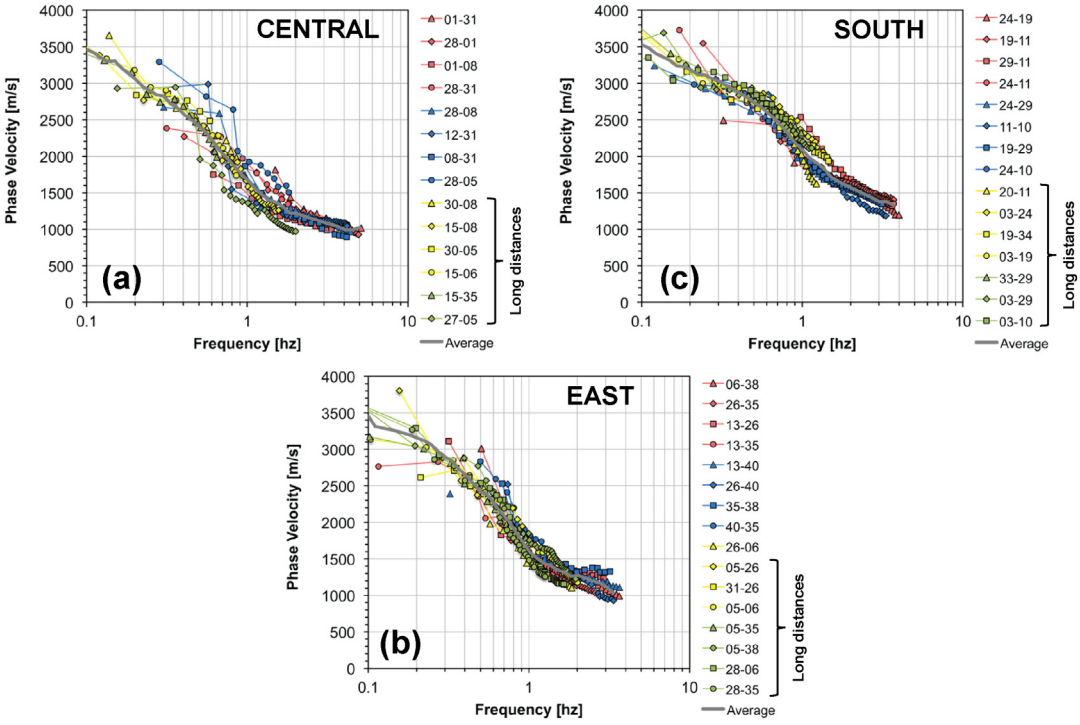

Fig. 7. Phase velocity dispersion curves for station pairs in the central (a), east (b), and south (c) districts (see Fig. 6). The solid gray lines are the average dispersion curves adopted for the inversion process, also plotted in Fig. 11.

The time-domain method is particularly useful when the frequency-domain method yields multiple physically-admissible solutions, and it does not resolve velocities at low frequencies. In such cases, the user must choose the "m" parameter (Eq. (1)) associated to a phase velocity curve that operated with Eq. (4) results in the best fit of the group velocity dispersion curve.

7. Shear wave velocity profiles

We used the average phase velocity dispersion curves, along with their standard deviations (not shown in the figures), calculated in the previous section to estimate representative shear wave velocity profiles for the three districts although we recognize that the shallower geomorphology of the east margin is more complex than those in the central and south districts.

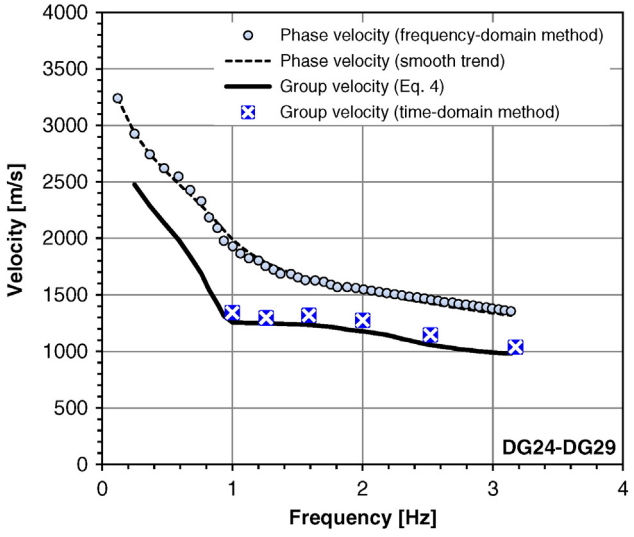

Fig. 8. Comparison of group velocities obtained from spectral and time-domain methods. The group velocity from the time-domain method is calculated as the average of the NCF causal and anti-causal parts.

We sought the simplest shear wave velocity (V_s) profiles that satisfy the dispersion curves in Fig. 7, using the software Dinver, a module for inversion problems based on a Neighbourhood Algorithm originally proposed by Sambridge (1999), and later improved by Wathelet (2008). Dinver software calculates, in addition to the shear wave velocity profile, the associated theoretical phase velocity dispersion curve of a multi-layer soil deposit. For the sake of simplicity, we explored simple two-layer models with an upper layer that increases in shear wave velocity with depth following a power law.

We used Monte Carlo simulations to generate 500,000 independent profiles and their corresponding theoretical dispersion curves for the fundamental mode of Rayleigh wave. Assuming the misfits between theoretical and measured dispersion curves follow a chi-square distribution, the ratio between the misfit of a given profile and the one of the optimum profile (minimum misfit) follows a Fisher distribution. For a confidence level of 10%, the misfit ratio is approximately 1.5 when a two layer model is adopted and the dispersion curve is discretized with 40 points (Socco and Boiero, 2008).

Flat H/V spectral ratios anticipate lack of pronounced impedance contrast between the soil and the underlying bedrock in the three districts. To account for the smooth transition, we adopted the same shear wave velocity domain for the three cases: a shallower layer whose velocity can vary following a power law with depth from 0.1–3 km/s at the surface to 0.2–5 km/s at the bottom and a uniform underlying layer with a shear wave velocity that can range from 2 to 7 km/s. We found the best overall data fit with 5 sub-layers for the shallower layer. The compressional wave velocity, Poisson's ratio, and density of the two layers were assumed constant given that they are second order variables (Wathelet, 2005).

The maximum analyzed depth z_{max} is set to a third of the longest wavelength λ_{max}, which was estimated as $\lambda_{max} = V_{max}/f_{min}$. The longest wavelength and maximum depth for the center, east, and south districts

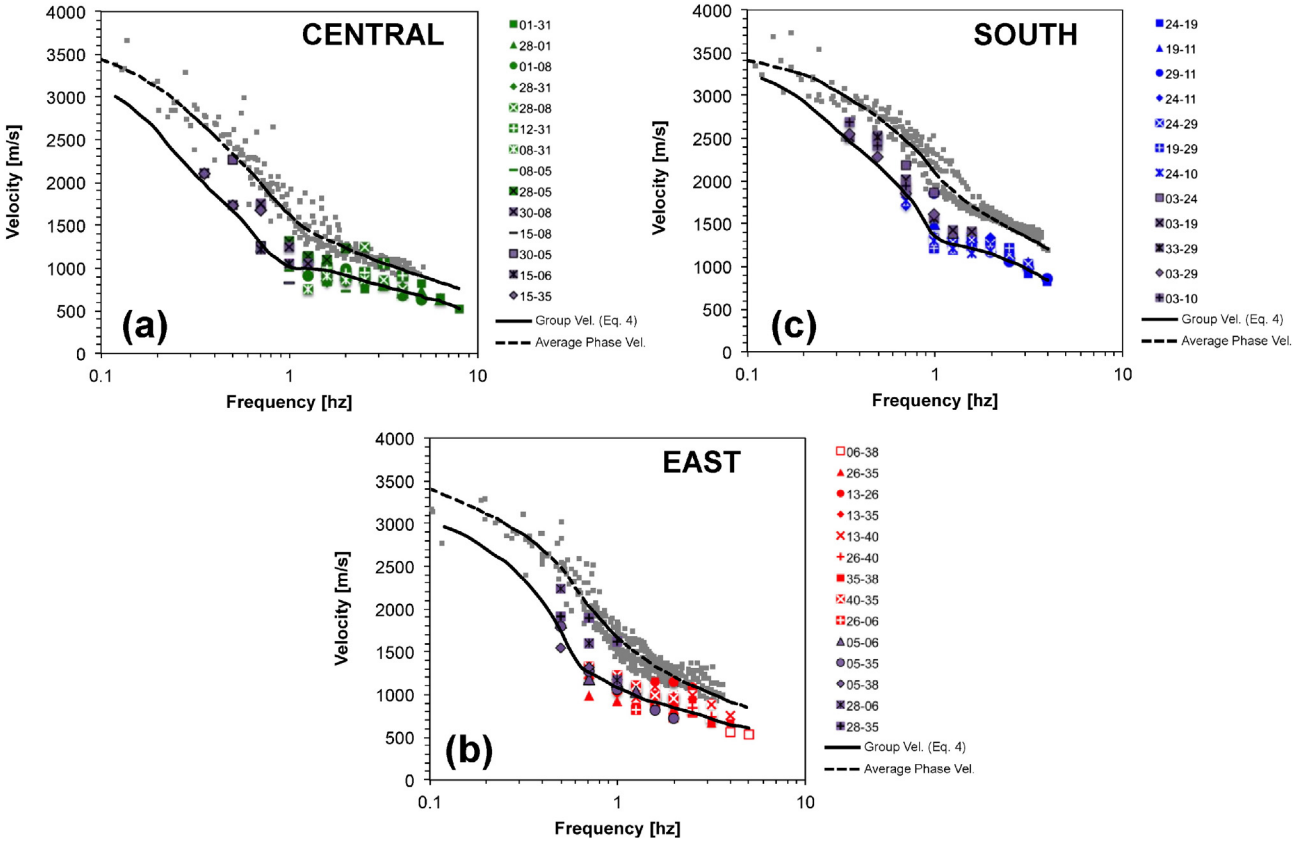

Fig. 9. Group and phase velocities in the central (a), east (b), and south (c) districts. The solid black lines are the group velocities calculated with Eq. (4) for the average dispersion curves in dotted lines. Small gray squares are phase velocities in Fig. 7.

are $\lambda_{max} = (3.4\ km/s)/(0.1\ Hz) \approx 34\ km$ and $z_{max} = \lambda_{max}/3 \approx 11\ km$, respectively.

Velocity profiles associated to dispersion curves obtained from the frequency-domain analyses in the central, east, and south districts are shown in Fig. 10. The minimum misfits are 0.73, 0.67, and 0.62, respectively. This figure shows all those profiles that have misfits smaller than 1.5 times the minimum misfit and represent equivalent profiles with a confidence level of 10%. The central and east districts profiles show a shear wave velocity of the shallower layer that increases from 700 m/s at the surface with a similar trend with depth. In contrast, the south district has a higher shallow shear wave velocity, but a similar V_s increase rate. All profiles predict a contact with the underlying homogeneous layer that is deeper than values proposed by the available gravimetric model of the basin (Yañez et al., 2015), ranging from 2.5 km in the south district to 4.5 km in the central. Fig. 11 shows the theoretical dispersion curves associated to the shear wave profiles along with the phase velocities calculated with the frequency-domain method.

The uppermost soil layer (first ~100 m depth) is not well resolved, given the lack of information at high frequencies in the dispersion

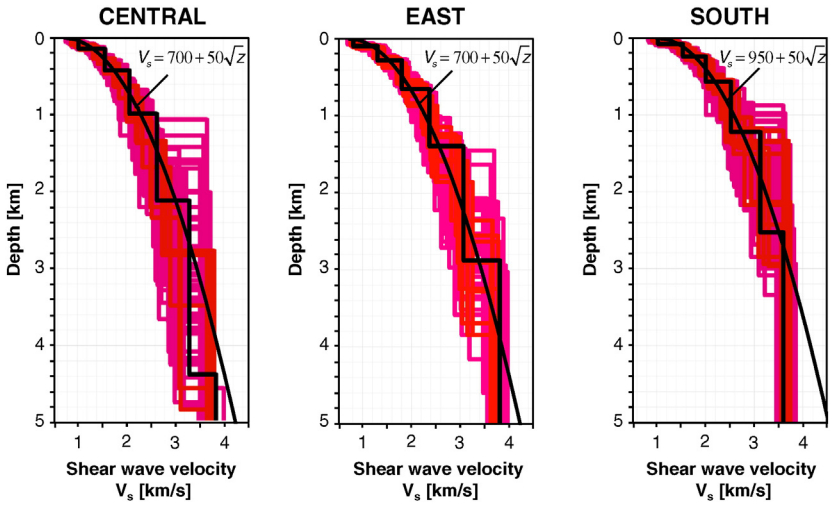

Fig. 10. Shear wave velocity profiles inverted from dispersion curves in the central (Fig. 7a), east (Fig. 7b), and south (Fig. 7c) districts. The profiles in black solid lines are the ones with minimum misfits while the rest are profiles with misfits lower than 1.5 times of the minimum. The Vs-models over the inverted profiles are smooth continuous trends discussed in the text.

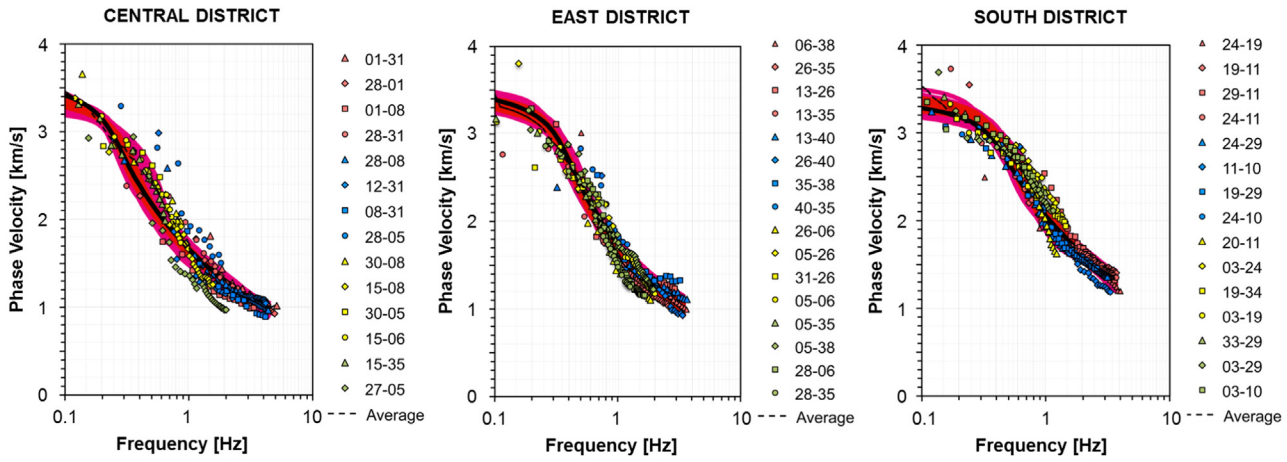

Fig. 11. Theoretical dispersion curves associated to shear wave velocity profiles in Fig. 10 along with measured phase velocities and the average dispersion curves in Fig. 7.

curves. However, this shallower information can easily be complemented with active or passive surface wave methods, such as SPAC, ESAC, and MASW (see examples for the Santiago Basin in Humire et al., 2015).

8. Discussion

The simple HVSR classification adopted for site characterization in this study intended identification of stiff soil deposits where the ambient seismic noise correlates. As the cross-correlation method is extended to softer soil deposits in future research, a more robust HVSR classification method, such as HVSR pattern recognition by cluster analysis (Panzera and Lombardo, 2013), should be adopted to properly interpret the results.

Inversion of single-station HVSR in the center of the basin resulted in a shear wave velocity profile that varies with the depth z [m] as $Vs\ (m/s) = 400 + 55\cdot(z)^{1/2}$, according to Pilz et al. (2010). This model can be slightly modified to fit the shear wave profile trends in Fig. 10. The models $Vs\ (m/s) = 700 + 50\cdot(z)^{1/2}$ and $Vs\ (m/s) = 950 + 50\cdot(z)^{1/2}$ are first order approximations of the inverted profiles in the central, east, and south districts. These high shear wave velocities agree with values as high as 1 km/s at 30 m depth reported for the Santiago gravel near the south district (Humire et al., 2015).

The underlying basement rocks are layered sequences of the Oligocene–early Miocene Abanico formation, the Lo Valle/Las Chilcas, and Veta Negra/Lo Prado formations (Armijo et al., 2010). According to a regional study conducted by Ward et al. (2013), a shear wave velocity near 3.5 km/s at 5 km depth can be inferred for the Santiago Basin area, which agrees well with the shear wave velocity of the underlying layer in the three profiles in the Fig. 10.

A compressional wave velocity (V_p) model derived from one-dimensional seismic refraction comprises three layers of 2.2, 6.7, and 6.1 km thick with average velocities of 4.9, 5.9, and 6.2 km/s (Godoy et al., 1999; Barrientos et al., 2004). The wave velocity of the shallower layer does not agree with the high velocities found in this study most likely due to the different scales of the estimations. While the Vp-model was defined from inter-station distances of hundreds of kilometers, our profiles resolve the shallower structure with a denser array.

9. Conclusions

A temporal network of broadband seismological stations was deployed in the Santiago Basin to perform intermediate to deep characterization of the soil deposits. We calculated cross-correlation of continuous vertical records of ambient seismic noise using spectral and time-domain methods. The spectral method resolves phase velocity dispersion curves whereas the time-domain method is suitable to obtain group velocities. Both methods combined resolve a frequency band (0.1–4 Hz) lower than that solved by traditional geotechnical surface wave methods. Stacking of short temporal windows improves resolution of the time-domain method in the higher frequency range, avoiding the use of whitening and temporal normalization.

Correlation between pairs of stations over stiff soil is stronger compared to correlation between pairs of stations over either soft-soft soils or stiff-soft soils. This lack of correlation can be anticipated in sites that exhibit single-station HVSR with pronounced peak amplitudes. Correlation in the time-domain shows strong directionality with higher SNR in west–east direction near the east bound of the basin.

We calculated representative phase velocity dispersion curves in three distinct city districts with dense station coverage and where we observed high inter-station correlation. The inverted shear wave velocity profiles show similarities between the central and the east districts in terms of shallow wave velocity and increase rate with depth. The velocity profile of the south district shows also a pronounced increase with depth, but a higher shallower velocity. The inversion process was not able to identify a clear soil-bedrock interface in the studied areas at depths predicted by available gravity-derived basement depth models.

Even though we emphasized deep characterization and could not resolve the shallowest soil structure, the high phase velocities calculated from station pairs over stiff Santiago Gravel agree well with the flat single-station HVSR calculated at the sites.

Acknowledgements

The authors would like to acknowledge the National Seismological Center (CSN) of the University of Chile for supporting the network deployment. We also thank Dr. G. Prieto for his helpful advice. This work was partly funded by the CONICYT-PCHA/Magíster Nacional/2014 – 22141523 and by the start-up fund from the Faculty of Physical and Mathematical Sciences and the Department of Civil Engineering at the University of Chile.

Appendix A. Supplementary data

Supplementary data to this article can be found online at http://dx.doi.org/10.1016/j.enggeo.2015.12.021.

References

Aki, K., 1957. Space and time spectra of stationary stochastic waves, with special reference to microtremors. Bull. Earthq. Res. Inst. 35, 415–457.

Armijo, R., Rauld, R., Thiele, R., Vargas, G., Campos, J., Lacassin, R., Kausel, E., 2010. The west andean thrust, the San ramón fault, and the seismic hazard for Santiago, Chile. Tectonics 29 (4), 1–34.

Astroza, M., Ruiz, S., Astroza, R., 2012. Damage assessment and seismic intensity analysis of the 2010 (Mw 8.8) Maule earthquake. Earthquake Spectra 28 (S1), S145–S164.
Bard, P.Y., Sesame-Team, 2004. Guidelines for the implementation of the H/V spectral ratio technique on ambient vibrations-measurements, processing and interpretations.
Barrientos, S., Vera, E., Alvarado, P., Monfret, T., 2004. Crustal seismicity in central Chile. J. S. Am. Earth Sci. 16 (8), 759–768.
Bensen, G., Ritzwoller, M., Barmin, M., Levshin, A., Lin, F., Moschetti, M., Shapiro, N., Yang, Y., 2007. Processing seismic ambient noise data to obtain reliable broad-band surface wave dispersion measurements. Geophys. J. Int. 169 (3), 1239–1260.
Boaga, J., Vaccari, F., Panza, G.F., 2010. Shear wave structural models of venice plain, Italy, from time cross correlation of seismic noise. Eng. Geol. 116 (3–4), 189–195.
Bonnefoy-Claudet, S., Cornou, C., Bard, P.Y., Cotton, F., Moczo, P., Kristek, J., Fäh, D., 2006. H/V ratio: a tool for site effects evaluation. Results from 1-D noise simulations. Geophys. J. Int. 167 (2), 827–837.
Bonnefoy-Claudet, S., Baize, S., Bonilla, L.F., Berge-Thierry, C., Pasten, C., Campos, J., Volant, P., Verdugo, R., 2009. Site effect evaluation in the basin of Santiago de Chile using ambient noise measurements. Geophys. J. Int. 176 (3), 925–937.
Boschi, L., Weemstra, C., Verbeke, J., Ekström, G., Zunino, A., Giardini, D., 2013. On measuring surface wave phase velocity from station–station cross-correlation of ambient signal. Geophys. J. Int. 192 (1), 346–358.
Charrier, R., Baeza, O., Elgueta, S., Flynn, J.J., Gans, P., Kay, S.M., Muñoz, N., Wyss, A.R., Zurita, E., 2002. Evidence for cenozoic extensional basin development and tectonic inversion south of the flat-slab segment, southern central andes, Chile (33°-36°S.L.). J. S. Am. Earth Sci. 15 (1), 117–139.
Díaz, D., Maksymowicz, A., Vargas, G., Vera, E., Contreras-Reyes, E., Rebolledo, S., 2014. Exploring the shallow structure of the San ramón thrust fault in Santiago, Chile (~33.5°S), using active seismic and electric methods. Solid Earth 5 (2), 837–849.
Ekström, G., 2014. Love and rayleigh phase-velocity maps, 5–40 s, of the western and central USA from USArray data. Earth Planet. Sci. Lett. 402, 42–49.
Ekström, G., Abers, G.A., Webb, S.C., 2009. Determination of surface-wave phase velocities across USArray from noise and Aki's spectral formulation. Geophys. Res. Lett. 36 (18), 5–9.
Godoy, E., Yañez, G., Vera, E., 1999. Inversion of an oligocene volcano-tectonic basin and uplifting of its superimposed miocene magmatic arc in the Chilean central andes: first seismic and gravity evidences. Tectonophysics 306 (2), 217–236.
Hannemann, K., Papazachos, C., Ohrnberger, M., Savvaidis, A., Anthymidis, M., Lontsi, A.M., 2014. Three-dimensional shallow structure from high-frequency ambient noise tomography: new results for the mygdonia basin-euroseistest area, northern Greece. J. Geophys. Res. Solid Earth 119 (6), 4979–4999.
Humire, F., Sáez, E., Leyton, F., Yañez, G., 2015. Combining active and passive multichannel analysis of surface waves to improve reliability of $V_{S,30}$ estimation using standard equipment. Bull. Earthq. Eng. 13 (5), 1303–1321.
Konno, K., Ohmachi, T., 1998. Ground-motion characteristics estimated from spectral ratio between horizontal and vertical components of microtremor. Bull. Seismol. Soc. Am. 88 (1), 228–241.
Leyton, F., Ruiz, S., Sepúlveda, S.A., 2010. Reevaluación del peligro sísmico probabilístico en Chile central. Andean Geol. 37 (2), 455–472.
Leyton, F., Sepúlveda, S.A., Astroza, M., Rebolledo, S., Acevedo, P., Ruiz, S., Gonzalez, L., Foncea, C., 2011. Seismic zonation of the Santiago Basin, Chile. Proceedings of Fifth International Conference on Earthquake Geotechnical Engineering.
Leyton, F., Ruiz, S., Sepúlveda, S.A., Contreras, J.P., Rebolledo, S., Astroza, M., 2013. Microtremors' HVSR and its correlation with surface geology and damage observed after the 2010 Maule earthquake (Mw 8.8) at talca and curicó, central Chile. Eng. Geol. 161, 26–33.
Luo, Y., Yang, Y., Xu, Y., Xu, H., Zhao, K., Wang, K., 2015. On the limitations of interstation distances in ambient noise tomography. Geophys. J. Int. 201 (2), 652–661.
Mordret, A., Landès, M., Shapiro, N., Singh, S., Roux, P., 2014. Ambient noise surface wave tomography to determine the shallow shear velocity structure at valhall: depth inversion with a neighbourhood algorithm. Geophys. J. Int. 198 (3), 1514–1525.
Nunziata, C., DE Nisco, G., Panza, G.F., 2009. S-waves profiles from noise cross correlation at small scale. Eng. Geol. 105 (3–4), 161–170.
Panzera, F., Lombardo, G., 2013. Seismic property characterization of lithotypes cropping out in the siracusa urban area, Italy. Eng. Geol. 153, 12–24.
Panzera, F., Pischiutta, M., Lombardo, G., Monaco, C., Rovelli, A., 2014. Wavefield polarization in fault zones of the western flank of Mt. Etna: observations and fracture orientation modelling. Pure Appl. Geophys. 171 (11), 3083–3097.
Picozzi, M., Parolai, S., Bindi, D., Strollo, A., 2009. Characterization of shallow geology by high-frequency seismic noise tomography. Geophys. J. Int. 176 (1), 164–174.
Pilz, M., Parolai, S., Picozzi, M., Wang, R., Leyton, F., Campos, J., Zschau, J., 2010. Shear wave velocity model of the Santiago de Chile basin derived from ambient noise measurements: a comparison of proxies for seismic site conditions and amplification. Geophys. J. Int. 182 (1), 355–367.
Poli, P., Pedersen, H., Campillo, M., 2012. Emergence of body waves from cross-correlation of short period seismic noise. Geophys. J. Int. 188 (2), 549–558.
Rebolledo, S., Lagos, J., Verdugo, R., Lara, M., 2006. Geological and geotechnical characteristics of the Pudahuel ignimbrite, Santiago, Chile. Proceedings of 10th IAEG International Congress. The Geological Society of London.
Sabra, K.G., Gerstoft, P., Roux, P., Kuperman, W., Fehler, M.C., 2005. Extracting time-domain green's function estimates from ambient seismic noise. Geophys. Res. Lett. 32 (3).
Sambridge, M., 1999. Geophysical inversion with a neighbourhood algorithm: I. Searching a parameter space. Geophys. J. Int. 138, 479–494.
Sánchez-Sesma, F.J., Campillo, M., 2006. Retrieval of the green's function from cross correlation: the canonical elastic problem. Bull. Seismol. Soc. Am. 96 (3), 1182–1191.
Shapiro, N.M., Campillo, M., 2004. Emergence of broadband rayleigh waves from correlations of the ambient seismic noise. Geophys. Res. Lett. 31 (7).
Shapiro, N.M., Campillo, M., Stehly, L., Ritzwoller, M.H., 2005. High-resolution surface-wave tomography from ambient seismic noise. Science 307 (5715), 1615–1618.
Shirzad, T., Shomali, Z.-H., 2014. Extracting seismic body and rayleigh waves from the ambient seismic noise using the rms-stacking method. Seismol. Res. Lett. 86 (1), 173–180.
Socco, L.V., Boiero, D., 2008. Improved monte carlo inversion of surface wave data. Geophys. Prospect. 56 (3), 357–371.
Stern, C.R., Amini, H., Charrier, R., Godoy, E., Herve, F., Varela, J., 1984. Petrochemistry and age of rhyolitic pyroclastic flows which occur along the drainage valleys of the Rio Maipo and Rio Cachapoal (Chile) and the Rio Yaucha and Rio Papagayos (Argentina). Rev. Geol. Chile (23), 39–52.
Stockwell, R.G., Mansinha, L., Lowe, R.P., 1996. Localization of the complex spectrum: the S transform. IEEE Trans. Signal Process. 44 (4), 998–1001.
Tsai, V.C., Moschetti, M.P., 2010. An explicit relationship between time-domain noise correlation and spatial autocorrelation (SPAC) results. Geophys. J. Int. 182, 454–460.
Udias, A., Madariaga, R., Buforn, E., 2014. Source Mechanisms of Earthquakes, theory and practice. Cambridge University Press, Cambridge, U.K. (p.).
Ward, K.M., Porter, R.C., Zandt, G., Beck, S.L., Wagner, L.S., Minaya, E., Tavera, H., 2013. Ambient noise tomography across the central andes. Geophys. J. Int. 194 (3), 1559–1573.
Wathelet, M., 2005. Array Recordings of Ambient Vibrations: Surface-Wave Inversion. Liege University, Belgium.
Wathelet, M., 2008. An improved neighborhood algorithm: parameter conditions and dynamic scaling. Geophys. Res. Lett. 35 (9).
Yañez, G., Muñoz, M., Flores-Aqueveque, V., Bosch, A., 2015. Gravity derived depth to basement in Santiago basin, Chile: implications for its geological evolution, hydrogeology, low enthalpy geothermal, soil characterization and geo-hazards. Andean Geol. 42 (2), 147–172.
Yang, Y., Ritzwoller, M.H., Levshin, A.L., Shapiro, N.M., 2007. Ambient noise rayleigh wave tomography across europe. Geophys. J. Int. 168 (1), 259–274.
Yao, H., Van der Hilst, R.D., Maarten, V., 2006. Surface-wave array tomography in SE Tibet from ambient seismic noise and two-station analysis – I. Phase velocity maps. Geophys. J. Int. 166 (2), 732–744.